machines

MDPI

Article

Sizing of the Motor Geometry for an Electric Aircraft Propulsion Switched Reluctance Machine Using a Reluctance Mesh-Based Magnetic Equivalent Circuit

Gayan Watthewaduge and Berker Bilgin *

Department of Electrical and Computer Engineering, McMaster University, Hamilton, ON L8S 4K1, Canada
* Correspondence: bilginb@mcmaster.ca

Abstract: The switched reluctance motor (SRM) is a promising candidate for electric propulsion systems. In the design process of an SRM, the motor geometry needs to be determined. Using the finite element method (FEM) might be time-consuming for the sizing of the motor geometry. As an alternative, electromagnetic models based on a magnetic equivalent circuit (MEC) can be utilized for the sizing of an SRM. MEC models require fewer computational resources and can help determine the electromagnetic performance with reasonable accuracy. Using the conventional MEC method for SRM sizing might be challenging since the flux pattern inside the motor should be changed for different motor dimensions. In order to address this challenge, this paper applies a reluctance mesh-based MEC technique to determine the geometry of a three-phase 12/16 SRM for a high-lift motor in the NASA Maxwell X-57 electric aircraft. A comprehensive reluctance mesh-based MEC model is developed for this purpose. Both the static and dynamic characteristics of the SRM geometry are evaluated using the reluctance mesh-based MEC method. The determined geometry is verified using the results computed from FEM.

Keywords: electric aircraft; magnetic equivalent circuit model; Maxwell Stress Tensor; propulsion motor; switched reluctance machine

Citation: Watthewaduge, G.; Bilgin, B. Sizing of the Motor Geometry for an Electric Aircraft Propulsion Switched Reluctance Machine Using a Reluctance Mesh-Based Magnetic Equivalent Circuit. *Machines* **2023**, *11*, 59. https://doi.org/10.3390/machines11010059

Academic Editor: Davide Astolfi

Received: 20 November 2022
Revised: 23 December 2022
Accepted: 27 December 2022
Published: 4 January 2023

1. Introduction

Electrified propulsion is expected to dominate future transportation systems due to the environmental impact of burning fossil fuels. Electric motors are on the path to replacing the engines energized by fossil fuels. Permanent magnet synchronous motors (PMSM) are already in use in electric propulsion systems [1]. The availability of materials and the reliability of the equipment are important factors in aircraft systems [2]. However, the permanent magnets (PMs) in PMSMs are sensitive to temperature, and they suffer from price volatility and supply chain issues [1,3]. The placement of PMs on the outer surface of the rotor or buried inside the rotor reduces the structural integrity of the motor. The switched reluctance motor (SRM) can overcome these drawbacks due to its magnet-free motor construction [4]. The absence of PMs eliminates price volatility and supply chain issues, and prevents thermal demagnetization faults, which allows an SRM to operate at higher temperatures. An SRM does not require a magnet retention system. Hence, the structural integrity of an SRM rotor is usually better than PMSMs. The above factors improve the fault tolerance capability of SRMs. Furthermore, SRMs have other advantages such as low cost and simple construction [3,4].

Designing an SRM for an electric propulsion system consists of multiple stages. Various electromagnetic models are used iteratively in each design stage [5]. Usually, the finite element method (FEM) is utilized in an SRM design. FEM can provide high accuracy, especially for nonlinear problems, and the capability to model complex geometries [4]. However, employing FEM models in all design stages can be time-consuming [6,7]. As an alternative, magnetic equivalent circuit (MEC) models can be applied for the sizing of an SRM [8]. The MEC modeling technique can account for local saturation, flux leakage, and multi-phase excitation in SRMs [9]. The accuracy of the MEC models is sufficient to determine the motor geometry [10].

One of the essential tasks in an SRM design process is to determine the motor geometry. The MEC method can be applied to size the motor geometry of an SRM as an alternative to the FEM. In refs. [11,12], MEC models were applied to design a wound field synchronous machine (WFSM) and a PMSM for electric vehicle applications. The MEC method is applied in [7,13] to design a flux switching machine for an in-wheel motor. The motor geometry of an axial flux SRM is obtained in [14,15], utilizing MEC models. However, the conventional MEC method implemented in [7,11–15] requires prior knowledge of the flux path inside the motor. The airgap flux paths in an SRM depend mainly on the pole configuration, geometry parameters and rotor position due to its salient structure. Therefore, it can be challenging to predefine the flux path accurately in an SRM, while modifying the motor geometry. Generally, presimulations are required in FEM to visualize the flux paths and make crude approximations to place airgap reluctance elements and calculate their reluctances [16]. The reluctance mesh-based MEC method is an alternative that does not require prior knowledge of the flux paths inside an SRM. In some cases, the higher number of reluctance mesh elements in the reluctance mesh-based method can cause a higher computation time than the conventional method. The computation time can be reduced by efficiently controlling the mesh densities [17]. In Ref. [18], we presented a comprehensive two-dimensional (2D) reluctance mesh-based MEC model for switched reluctance machines. The MEC models of three-phase 6/4, 6/16, and 12/8, and four-phase 8/6, 8/10, and 16/12 SRMs were implemented in [18]. The static and dynamic characteristics of those SRMs from MEC models were validated both with 2D FEM and experimental tests. The static and dynamic characteristics obtained from the proposed reluctance mesh-based MEC method has a good accuracy according to the FEM and experimental results in [18]. The reluctance mesh-based MEC method has not been applied to the sizing of the motor geometry of SRMs even though it can overcome the issues of the conventional MEC method. In this paper, the reluctance mesh-based MEC method presented in [18] is applied to the sizing of a three-phase 12/16 SRM for the performance requirements of the NASA high-lift motor (HLM) for the Maxwell X-57 aircraft [19]. The static and dynamic characteristics of the identified SRM geometry from the reluctance mesh-based MEC method are validated with FEM results.

The rest of the paper is organized as follows. The design specifications of the HLM and the motor geometry of the proposed 12/16 SRM are presented in Section 2. In Section 3, the reluctance mesh-based MEC method and its field solution techniques are described. Section 4 validates the static characteristics of the proposed SRM derived from the MEC method using the FEM results. Section 5 shows the MEC-based dynamic characteristics of the proposed SRM and compares them with the results from FEM. Finally, Section 6 presents the conclusions of the paper.

2. NASA Maxwell X-57 Electric Aircraft

This paper applies a reluctance mesh-based MEC technique to identify the geometry of a three-phase 12/16 SRM for a high-lift motor in the NASA Maxwell X-57 electric aircraft. In this section, first, the NASA Maxwell X-57 aircraft is presented, and then, the design specifications for the NASA high-lift motor for the Maxwell X-57 aircraft are introduced.

2.1. NASA Maxwell X-57 Aircraft

The NASA Maxwell X-57 aircraft consists of a distributed electrical propulsion system. The main objectives for the Maxwell X-57 are to reduce the energy consumption during the cruise, achieve zero carbon emissions, and decrease the noise. The total propulsion power of the aircraft is provided by 14 electric motors, as shown in Figure 1 [19]. The two large motors at the corners of the left and right wings mainly produce the power for cruising. The remaining 12 motors are the high-lift motors (HLMs). HLMs are mounted on the left and right wings, and they operate during the flight take-off and landing. The HLMs are not operated during the cruise to reduce air drag. These 12 HLMs should ensure the climbing of the aircraft up to a maximum altitude of 3 km above sea level. The expected minimum operation time of the HLMs during the climbing stage is approximately 250 s. Furthermore, there is a run-up for 30 s at the beginning of the flight mission where the motors run at 4000 r/min.

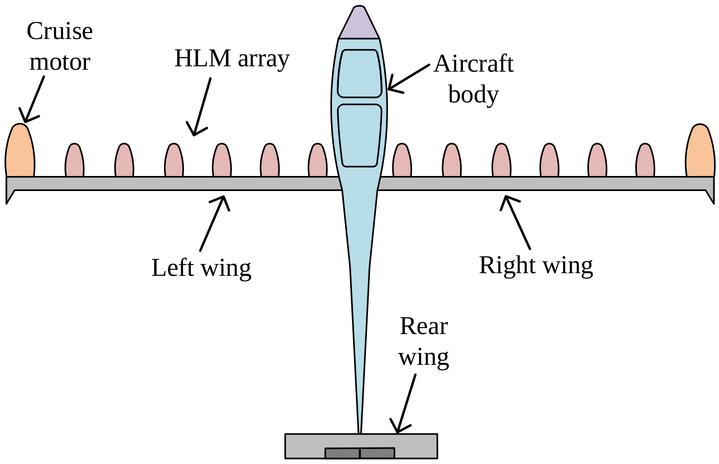

Figure 1. Top view of the NASA Maxwell X-57 distributed propulsion aircraft [19].

2.2. Design Specifications of the HLM

For the given operating scenarios, the electrical and physical requirements for HLM defined by NASA are shown in Table 1 [19,20]. NASA has already designed a PMSM to achieve the above requirements. The outer diameter of the PMSM was 156.45 mm. The maximum available axial length for the stator (including the stack length of the stator core and the length of the end turns) was defined as 66.4 mm. The stator design of the PMSM achieves a stack length of 34.5 mm by using a 24 slot–20 pole PMSM design. The torque density of the PMSM has been greatly improved by using a Halbach magnet array. This also helped to reduce the rotor back-iron thickness of the PMSM to 2.45 mm, leading to further weight reduction. The maximum magnet temperature was considered to be 120 °C . The stator and rotor laminations are bonded using EB-548 epoxy. The maximum allowable temperature of the EB-548 is 140 °C. Based on these temperature constraints, the maximum current density of the PMSM is limited to 11 A/mm^2. The maximum wire fill factor and current density requirements, as well as the achieved fill factor and current density for the PMSM design, are shown in Table 2.

Table 1. Main design specifications of an HLM.

Electromagnetic Design Parameters	
Peak output power	13.7 kW
Peak torque	24 N·m
Minimum torque density	18.8 N·m/L
Base speed	5450 r/min
RMS phase current	35 A
DC link voltage	385–538 V
Number of phases	3

Table 1. *Cont.*

Geometry Constraints	
Maximum motor diameter (with casing)	161.5 mm
Maximum stator outer diameter (without casing)	156.45 mm
Maximum stator axial length including end turns	66.4 mm
Expected Performance	
1. Provide 24 N·m of torque between 2000 and 5450 r/min and 22 N·m of torque at 5460 r/min.	
2. Capable of producing 10.5 kW output power at 5460 r/min and at 460 V DC link voltage with a minimum efficiency of 93%.	

Table 2. Fill factor and current density constraints.

Characteristic	Maximum Allowable Value	Achieved by PMSM Design
Wire fill factor	60%	58.4%
Current density	11 A/mm^2	10.7 A/mm^2

3. Reluctance Mesh-Based MEC Model

This section discusses applying the reluctance-mesh-based MEC technique to obtain the electromagnetic model of the proposed 12/16 SRM. Utilizing the developed MEC model for calculating the static and dynamic characteristics is also explained.

3.1. Developing the Reluctance Mesh-Based MEC Model

Reluctance mesh is created in the magnetic domain by decomposing the SRM geometry into mesh elements, as shown in Figure 2 [18]. The mesh element densities in different geometry regions are varied by changing the number of radial and tangential segments. The shape of each mesh element is arc-shaped. The effect of the magnetic saturation in the stator and rotor core can be accounted for accurately by calculating the relative reluctivity in the mesh elements of the stator and rotor core. In meshing, the mesh element densities in the stator and rotor core regions are increased sufficiently to improve the local saturation effect in the motor core. In Figure 2, the arc angle of the airgap mesh elements is 1.875°, which is the same as the rotating step angle of the rotor. The airgap is segmented into two layers along the radial direction. The elements in the layer next to the rotor move with the rotor, and elements next to the stator do not rotate. Smaller arc angles in the airgap mesh elements help achieve smoother magnetic field distribution in the airgap and reduce the simulation time step. Arc angles of the elements in the other regions should always be multiples of the arc angle of airgap mesh elements. The height of the mesh elements along the radial direction can be controlled by changing the number of radial segments. The arc length and height of stator and rotor pole mesh elements should be sufficiently small to capture the local saturation in the poles. In this example, the arc angles of rotor pole mesh elements are the same as airgap mesh elements to reduce the complexity of the meshing. The arc angles of the stator pole mesh elements are two times higher than the airgap mesh elements. There are four radial divisions in both stator and rotor pole regions. Generally, stator and rotor back-iron experience lower saturation compared to the stator and rotor poles. Thus, the number of mesh elements in the stator and rotor back-iron regions is not necessarily as high as in the stator and rotor poles. Therefore, arc angles have been chosen four times higher in the stator and rotor back-iron regions. The radial divisions are considered to be two and three for the mesh elements in the stator and rotor pole regions. The reluctance mesh in Figure 2 can be further adjusted based on the accuracy of the results and computational time of the model.

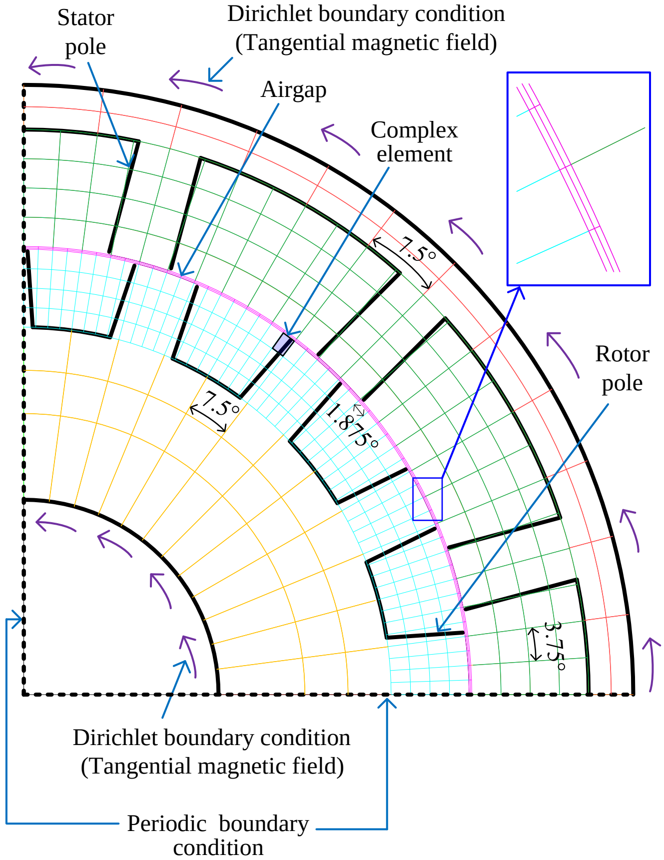

Figure 2. An example reluctance mesh for 12/16 SRM [18].

Figure 3 shows the reluctance elements and arrangement of MMF sources inside the mesh elements in Figure 2. The length and height of the mesh elements are $2l$ and $2h$, respectively. The variables l and h denote the length and height. The axial length of the mesh element is denoted by a. As shown in Figure 3, there are four reluctance elements connected to the center node of the mesh element. Two reluctance elements are along the radial direction and have the same reluctance R_1, equal to $(\nu h/la)$. The other two reluctance elements are along the tangential direction with reluctance R_2, equal to $(\nu l/ha)$. The variable ν represents the reluctivity of the mesh element. In Figure 3, two MMF sources, F_{s1} and F_{s2}, exist along the radial direction. The MMF values of the sources corresponding to the mesh elements in the stator back-iron, rotor, and airgap are zero. There are non-zero MMFs for the mesh elements in stator poles and slots.

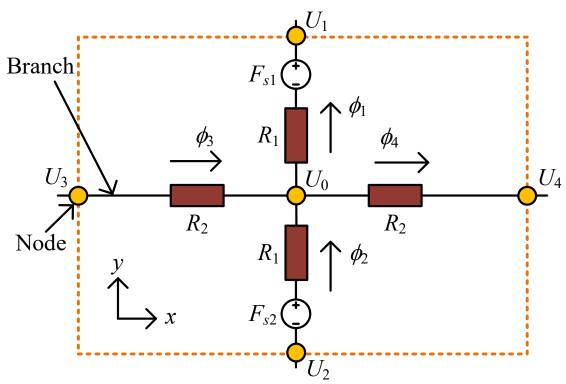

Figure 3. Structure of a reluctance mesh element and MMF source arrangement.

The magnetic scalar potentials of the central node and four boundary nodes in Figure 3 are U_0, U_1, U_2, U_3, and U_4, respectively. The nodal equation as a function of the magnetic scalar potential, MMF, and reluctance can be expressed as

$$\left(\frac{U_1 - U_0 - F_{s1}}{R_1} + \frac{U_2 - U_0 + F_{s2}}{R_1}\right) + \left(\frac{U_3 - U_0}{R_2} + \frac{U_4 - U_0}{R_2}\right) = 0. \tag{1}$$

The branch fluxes across each reluctance element in Figure 3 are ϕ_1, ϕ_2, ϕ_3 and ϕ_4.

3.2. Solution of the Magnetic Field

The branch fluxes of all mesh elements in the geometry are needed to obtain the field solution. The loop analysis technique is applied here to calculate the branch fluxes.

For current excitation, the following nonlinear matrix equation is solved iteratively [18]:

$$\boldsymbol{r} = \boldsymbol{R}\boldsymbol{\phi}_l - \boldsymbol{F}_l \tag{2}$$

where $\boldsymbol{R} \in \mathbb{R}^{n_l \times n_l}$ is the reluctance network matrix. The vectors $\boldsymbol{\phi}_l \in \mathbb{R}^{n_l \times 1}$ and $\boldsymbol{F}_l \in \mathbb{R}^{n_l \times 1}$ are the loop flux and loop MMF vectors, respectively. $\boldsymbol{r} \in \mathbb{R}^{n_l \times 1}$ is the residual vector. Variable n_l is the number of loops in the MEC model.

For voltage excitation, the phase flux linkage vector $\boldsymbol{\psi} \in \mathbb{R}^{m \times 1}$, loop flux vector $\boldsymbol{\phi}_l$, and phase current vector $\boldsymbol{I}_s \in \mathbb{R}^{m \times 1}$ can be calculated by solving [18]:

$$\boldsymbol{\psi} = \int \left(\boldsymbol{V}_{ph} - \boldsymbol{R}_s \boldsymbol{I}_s\right) dt \tag{3}$$

$$\boldsymbol{r}_e = \begin{bmatrix} \boldsymbol{R} & -s_f \boldsymbol{N} \\ p\boldsymbol{N}^T & \boldsymbol{0} \end{bmatrix} \begin{bmatrix} \boldsymbol{\phi}_l \\ \boldsymbol{I}_s \end{bmatrix} - \begin{bmatrix} \boldsymbol{0} \\ \boldsymbol{\psi} \end{bmatrix} \tag{4}$$

where $\boldsymbol{V}_{ph} \in \mathbb{R}^{m \times 1}$, $\boldsymbol{r}_e \in \mathbb{R}^{(m+n_l) \times 1}$ are the phase voltage vector and extended residual vector, respectively. $\boldsymbol{R}_s \in \mathbb{R}^{m \times m}$ is the phase resistance matrix where the resistance of each phase is included in the diagonal elements of the matrix. $\boldsymbol{N} \in \mathbb{R}^{n_l \times m}$ is the winding function matrix that represents the summation of the winding function values corresponding to the MMF sources of the mesh elements around each loop [18]. The variables p and m are the number of magnetic poles and the number of phases of the SRM. The variable s_f is the scaling factor to avoid poor conditions during the iterative solution process.

The process of implementing dynamic simulation while considering magnetic saturation and mutual coupling effects is shown in Figure 4. The electrical angle θ_{elec} is computed using the given motor speed, N_{rpm}, and the number of rotor poles, N_r, as shown in Figure 4. Phase shift between the phases is included to θ_{elec} to calculate the electrical angle of each phase. The current is regulated at a given reference, I_{ref}, using a hysteresis controller with a hysteresis band, ΔI. The θ_{ON} and θ_{OFF} of the phases are given as an input to the hysteresis current controller. The current controller turns the phases on and off according to the given turn-on angle, θ_{ON}, and turn-off angle, θ_{OFF}. According to the input phase currents, $\boldsymbol{I}_s$ at the k^{th} iteration, I_{ref}, θ_{ON}, and θ_{OFF}, phase voltages $\boldsymbol{V}_{p,k}$ are applied to the MEC model. Hence, phase flux linkages at the next iteration are determined by solving Equation (3). Then, $\boldsymbol{I}_s$ and $\boldsymbol{\phi}_l$ can be calculated by Equation (4) using the iterative procedure in Figure 4 [18]. Initially, zero vectors are assigned to both $\boldsymbol{I}_s$ and $\boldsymbol{\phi}_l$. The relative reluctivity, $\boldsymbol{\nu}_r$, of nonlinear materials is considered to be unity at first. The matrices $\boldsymbol{N}$ and $\boldsymbol{R}$ are then built, and the Jacobian and Hessian matrices are calculated. Next, the values of $\boldsymbol{I}_s$ and $\boldsymbol{\phi}_l$ at the $(\text{k+1})^{\text{th}}$ are calculated using the Gauss Newton method [18]. Then, the relative reluctivity of nonlinear mesh elements is recalculated for the $\boldsymbol{\phi}_l$ at the $(\text{k+1})^{\text{th}}$. The convergence criteria are checked. If $\boldsymbol{r}_e$ is less than the tolerance ϵ, the iterative procedure is stopped. Otherwise, the relative reluctivity of nonlinear elements is obtained again using the BH characteristics of the utilized steel material in the core and matrix $\boldsymbol{R}$ is rebuilt. The iterative procedure continues until it satisfies the convergence criteria. The phase currents, self, and mutual flux linkage during the phase commutation are considered in Equation (3). Then, the self and mutual flux linkage calculated in Equation (3) are used in Equation (4) to account for the phase interaction effects while solving for the phase currents.

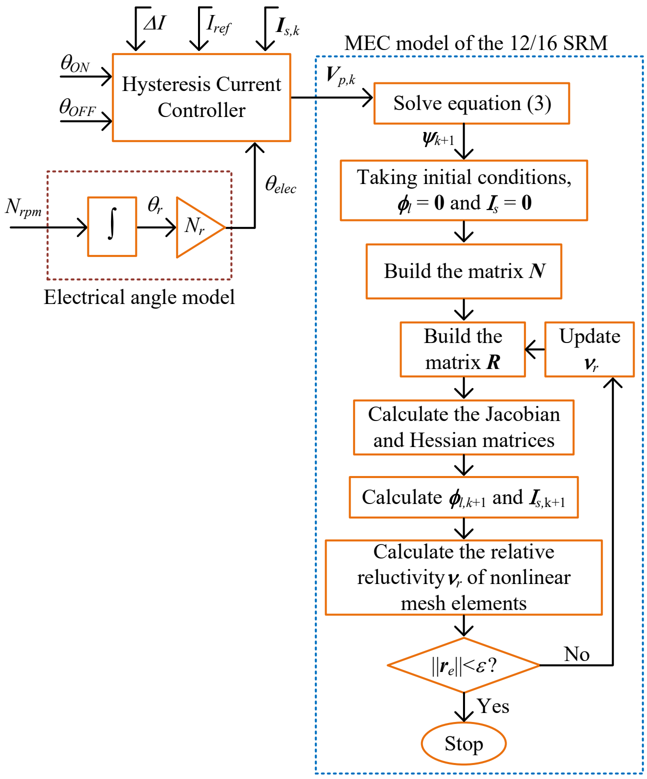

Figure 4. The procedure for implementing the dynamic model, including the magnetic saturation effects and mutual coupling.

4. Sizing of the SRM Geometry Using the Proposed Reluctance Mesh-Based MEC Method

In this section, the sizing of the SRM is discussed. The techniques of selecting the pole configuration, geometry parameters, winding configuration, and the magnetic material are explained.

4.1. Selection of the Pole Configuration

According to the dimensional constraints given by NASA, HLM requires a higher torque to volume ratio. Therefore, flux density in the stator core should be closer to the saturation flux density of the utilized steel material to increase the torque density. In this application, the maximum wire fill factor in the stator slots is constrained to 60%. The motor should have only three phases, according to NASA specifications. Considering the geometry and fill factor constraints, choosing a high stator pole count might limit the slot area. This could further reduce the MMF, leading to lower torque production. The stator outer diameter is constrained to 156.45 mm, as listed in Table 1. The possible number of stator poles for a three-phase SRM is a multiple of six, such as 6, 12, 18, and 24. For six stator poles, there will be only two magnetic poles in the motor. Therefore, the SRM may require thicker stator back-iron to avoid oversaturation in the stator core. A higher stator back-iron thickness can reduce the copper fill factor due to a smaller stator slot area for the given stator outer diameter. A lower copper fill factor decreases the MMF and reduces the torque production. For 12 stator poles, there will be four magnetic poles that require less magnetic flux carrying capability in the stator back-iron. Furthermore, the PMSM designed by NASA achieves thinner stator back-iron thickness using 24 stator slots. Moreover, a number of stator slots such as 18 or 24 would limit the stator slot area.

This can decrease the copper fill and reduce the torque production capability due to less MMF production. Figure 5 shows the static electromagnetic torque at 60 A excitation for three-phase 6/16, 12/16, and 24/16 SRMs. For comparison purposes, all three SRMs in Figure 5 have similar dimensions and the same MMF is applied to them. The average torque of static torque profiles in Figure 5 for 6/16, 12/16, and 24/16 SRMs is 16.6 Nm, 20.1 Nm, and 18.9 Nm, respectively. Therefore, the design with 12 stator poles has a higher torque production capability. For the NASA HLM application, 12 stator poles would be a better choice to achieve a thinner stator back-iron to maximize the torque density. Considering these reasons, the number of stator poles is selected as 12.

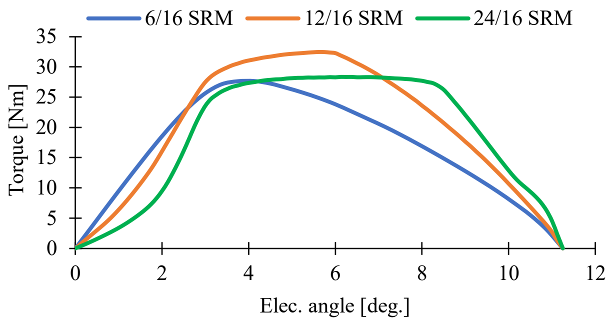

Figure 5. Static electromagnetic torque at a 60 A excitation current for 6/16, 12/16, and 24/16 SRMs.

There are various options for the number of rotor poles that would provide a balanced three-phase operation with 12 stator poles. The possible numbers of rotor poles are 8, 16, and 20 [21]. The numbers of torque pulsations for the considered number of rotor poles are 24, 48, and 60, respectively. The main operating speed of the motor is 5450 r/min according to Table 1. The electrical frequencies of the considered numbers of rotor poles at 5450 r/min are 726.67 Hz, 1453.33 Hz, and 1816.7 Hz, respectively. The lower number of torque pulsations can increase the torque ripple and higher electrical frequencies can increase the losses. Moreover, a lower number of rotor poles results in wider stator poles that require thicker stator back-iron. Hence, this reduces the copper fill factor and decreases the torque production capability. A higher number of rotor poles results in higher core loss and narrower stator poles that can over saturate both stator and rotor poles. Figure 6 shows the static electromagnetic torque of 12/8, 12/16, and 12/20 SRMs at a 60 A excitation current. The same MMF is provided for all three SRMs. The outer diameter, stator bore diameter, and stator and rotor pole heights are the same. The average static torque for 12/8, 12/16, and 12/20 SRMs are 17.8 Nm, 20.1 Nm, and 19.1 Nm, respectively. Therefore, the design with 16 rotor poles has a higher torque production capability.

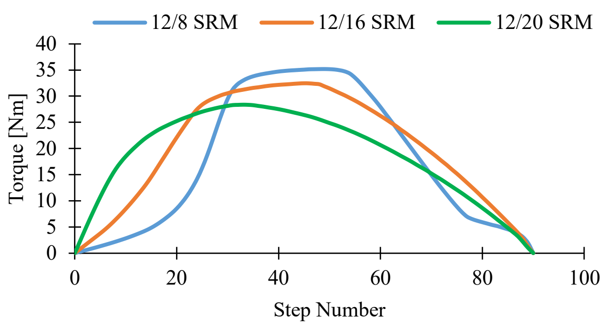

Figure 6. Static electromagnetic torque at a 60 A excitation current for 12/8, 12/16, and 12/20 SRMs.

For the given speed range and the stator outer diameter, 16 rotor poles are a better choice to maintain an effective stator pole width considering torque density, and a reasonable electrical frequency considering core loss for the given speed range.

4.2. Selection of Geometry Parameters

The geometry design parameters of the three-phase 12/16 SRM are shown in Figure 7. The motor geometry is determined to achieve the maximum torque requirement at the minimum DC link voltage of 385 V. According to the given specifications in Table 1, the maximum outer diameter of the motor with the casing should be 161.5 mm. The stator outer diameter is set at 156.45 mm, which is the same as the PMSM designed by NASA for the HLM application.

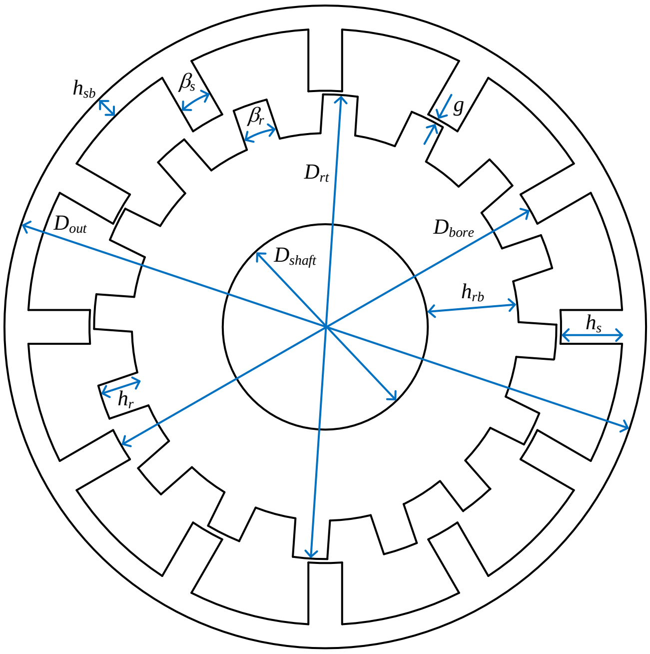

Figure 7. Main geometry parameters of the 12/16 SRM.

An SRM requires a smaller airgap to achieve high torque density. For the HLM, 0.3 mm, 0.35 mm, and 0.4 mm airgap lengths are considered. The dynamic electromagnetic torque calculated from the MEC model for those three airgaps is shown in Figure 8 and the average torque and torque ripple are shown in Table 3. As shown in Table 3, a 0.4 mm airgap is not sufficient to achieve the minimum torque density of 18.8 N·m/L. Both 0.35 mm and 0.3 mm airgaps exceed the torque density requirement. The airgap length of 0.4 mm has the minimum torque ripple. Tighter tolerances would be needed for a 0.3 mm airgap compared with 0.35 mm. Therefore, the airgap length is selected as 0.35 mm. An airgap length of 0.35 mm would still require tight tolerance when manufacturing the core and other mechanical parts of the motor. For an industrial application, this would potentially be reflected as a higher cost. However, for an aircraft application, cost is usually a lower priority than torque density.

Table 3. Average torque and torque ripple of the torque profiles in Figure 8.

Airgap Length	Avg. Torque	Pk–Pk Torque Ripple	Torque Density
0.4 mm	23.6 N·m	14 N·m	18.5 N·m/L
0.35 mm	24.6 N·m	14.59 N·m	19.3 N·m/L
0.3 mm	25.5 N·m	15.23 N·m	20 N·m/L

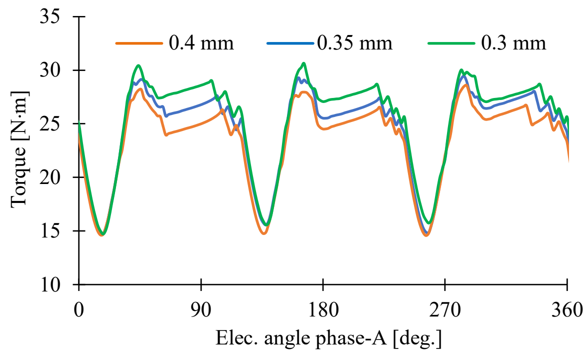

Figure 8. Dynamic electromagnetic torque from the MEC model at 5450 r/min at different airgaps.

The maximum and the minimum limits of the pole arc angles are calculated according to

$$\beta_r + \beta_s \leq \frac{360^\circ}{N_r} = 22.5^\circ \quad (5)$$

$$\beta_r + \beta_s \geq \frac{720^\circ}{mN_r} = 15^\circ \quad (6)$$

where β_s, β_r, N_r, and m are the stator pole arc angle, rotor pole arc angle, number of rotor poles, and number of phases, respectively, [3]. Equation (5) ensures the existence of a fully unaligned position. Equation (6) is the minimum condition of pole arc angles for the self-starting condition in SRMs. Initially, both β_r and β_s were chosen as 7.5° to satisfy Equation (6) . After that, the phase current and electromagnetic torque were calculated at 5450 r/min using the MEC model. If the average torque and rms phase current did not satisfy the requirements, the values of the pole arc angles were modified, and torque and phase currents were calculated again. This process was repeated until the torque and rms phase current requirements were satisfied. The final values of the stator and rotor pole arc angles were 8.2° and 8.5°, respectively.

The stator pole height is selected to maximize the slot area while achieving the 24 N·m torque requirement at 5450 r/min within the maximum rms current limit of 35 A and 60% fill factor constraint. Figure 9 shows the static torque profiles at a 60 A excitation current for various rotor pole heights. The torque production capability of the 12/16 SRM reduces at lower rotor pole heights. This is because with a lower rotor pole height, a significant amount of flux penetrates into the back-iron instead of the rotor pole. The final rotor pole height was selected as 10 mm, as there was no significant improvement in the torque when the rotor pole height is above this value.

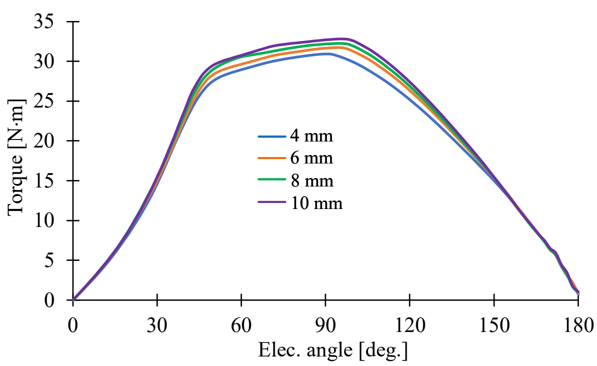

Figure 9. Static torque profiles at a 60 A excitation current for different rotor pole heights.

The stator back iron of the PMSM designed for the HLM application was approximately 3 mm due to the high torque–density requirement. In the SRM, the stator back-iron thickness should be selected to avoid oversaturation. The stator back-iron should be capable of carrying nearly half of the flux flowing in the stator pole. Therefore, the minimum stator back-iron thickness should be at least half of the stator pole width. Furthermore, the stator back-iron should provide a better structural support to the stator poles to avoid the oversaturation of the back iron. The stator pole width of the HLM is 8.22 mm. Therefore, the stator back-iron thickness is kept higher than 4.11 mm. The rotor back-iron thickness is determined according to the rotor pole height and the shaft diameter [3,22]. The shaft diameter of the 12/16 SRM design is 50 mm. The final values for the motor geometry parameters of the 12/16 SRM design for the HLM application are given in Table 4.

Table 4. Proposed dimensions of the SRM geometry.

Parameter	Value
Outer diameter (D_{out})	156.45 mm
Bore diameter (D_{bore})	115 mm
Shaft diameter (D_{shaft})	50 mm
Airgap length (g)	0.35 mm
Stator pole arc angle (β_s)	8.2°
Rotor pole arc angle (β_r)	8.5°
Stator pole height (h_s)	15 mm
Rotor pole height (h_r)	10 mm
Stator back-iron thickness (h_{sb})	5.725 mm
Rotor back-iron thickness (h_{rb})	22.15 mm

4.3. Material for the Magnetic Cores

For the 12/16 SRM design, it is essential to achieve higher flux density in the airgap to maximize the torque density [19]. The utilized magnetic steel material should have a higher saturation flux density. Cobalt–iron (CoFe) magnetic materials provide the highest saturation flux density level as compared to the other technologies in the market [1]. Hiperco-50 [23], AFK-502 [24], and Vacodur-49 [25] are considered as potential CoFe soft magnetic materials for the stator and rotor of the HLM. The HLM is not a high-speed motor, and the maximum operating speed is around 6000 r/min [19]. Thus, the material properties are considered for annealing for optimum magnetic properties. Additionally, non-oriented electrical steel 35JN210 from JFE is considered for comparison [26]. Some of the critical properties of these materials are shown in Table 5. The static electromagnetic torque with different materials at a 60 A excitation current is shown in Figure 10. As shown in Figure 10, all three CoFe materials have similar static torque characteristics. The 35JN210 has lower torque production capability due to the lower saturation flux density of 1.65 T [26]. All three CoFe materials have similar electrical resistivity and thermal conductivity, as shown in Table 5. Hiperco-50 has the lowest specific core loss and AFK-502 has the highest yield strength. However, Hiperco-50 can have 414 MPa yield strength after annealing the material for the optimum mechanical properties. The yield strength of the Hiperco-50 is closer to 420 MPa, which is the maximum yield strength of AFK-502. By considering both magnetic and mechanical properties, Hiperco-50 iron–cobalt–vanadium soft magnetic alloy from Carpenter technology is chosen as the magnetic core lamination material for both stator and rotor. The 0.15 mm-thick Hiperco-50 lamination is used for the sizing of the 12/16 SRM. The *B-H* curve and specific core losses of the lamination are shown in Figure 11.

Table 5. Magnetic, thermal, and mechanical characteristics of the cobalt–iron materials [23–25].

Characteristic		Hiperco-50	AFK-502	Vacodur-49
Specific core loss	400 Hz/2 T	56.7 W/kg	70 W/kg	60 W/kg
	1000 Hz/2 T	301 W/kg	320 W/kg	330 W/kg
Saturation flux density		2.3 T	2.32 T	2.3 T
Resistivity		0.4 μΩ · m	0.4 μΩ · m	0.42 μΩ · m
Yield strength		331 MPa–414 Mpa	300 MPa–420 Mpa	210 MPa–390 Mpa
Thermal conductivity		29.8 W/m·K	32 W/m·K	32 W/m·K

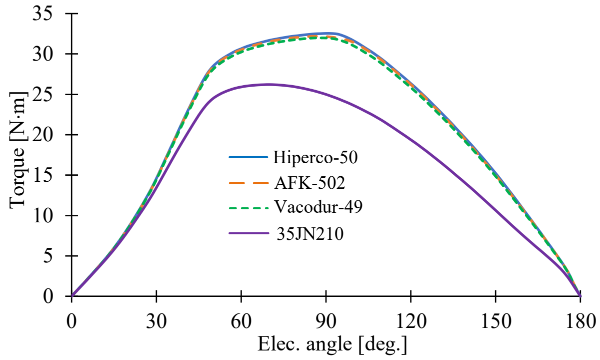

Figure 10. Static torque profiles at a 60 A excitation current for different magnetic materials.

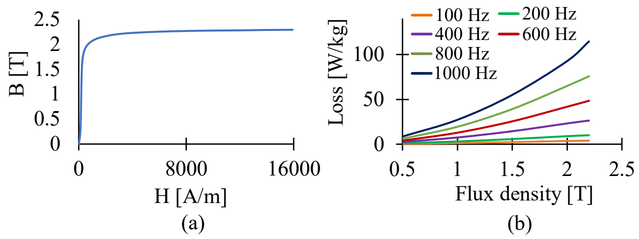

Figure 11. Characteristics of Hiperco-50 0.15 mm laminations: (**a**) *BH* characteristics and (**b**) specific core losses.

4.4. Selection of Winding Configuration and Stack Length

There are four coils per phase in a three-phase 12/16 SRM. For this application, all four coils are connected in series. The number of turns should be sufficient to create the required MMF in the airgap. The maximum number of turns of a coil is limited by the maximum slot fill factor, wire size, DC link voltage constraint, current dynamics, and phase resistance or copper loss [22]. The HLM design needs to deliver 24 N·m of torque at 5450 r/min. From the SRM design perspective, this would require a minimum 24 N·m peak static torque around a 50 A excitation current to satisfy the RMS current constraint. Furthermore, the peak static induced voltage needs to be within 385–538 V at 5450 r/min. As shown in Table 1, the maximum available stator axial length including the end turn lengths is constrained at 66.4 mm. After analyzing the static torque characteristics of the SRM design with different numbers of turns per coil and stator core stack length in various iterations, and checking the dynamic performance of the motor with the MEC model, the number of turns per coil is selected as 32 and the stator core stack length is selected as 47 mm. The end turn length on each side of the coil is estimated as 9.7 mm. This makes the total axial length of the stator 66.4 mm, which is within the design constraint defined in Table 1. Different wire gauges with different numbers of strands are considered to achieve the wire fill factor constraint of 60% and the current density limit of 11 A/mm^2. With 32 turns and three strands per coil wound with 17 AWG heavy-build magnet wire, the 12/16 SRM achieves

24 N·m at 5450 r/min with an RMS current of 34.3 A at the minimum DC link voltage of 385 V. The SRM achieves this requirement at an RMS current density of 10.96 A/mm^2 with a fill factor of 58.4%, which are lower values than the design constraints defined in Table 2. The parameters of the selected winding configuration and stack length are provided in Table 6. The mass of the stator core, rotor core, and coils is 1.53 kg, 2.33 kg, and 1.77 kg, respectively. The total mass of the electromagnetic components is 5.63 kg. The rotor mass can be further reduced by adding cut outs in the rotor back-iron. The same IEEE 95-2002 standard used in the PMSM design is considered for selecting the thickness of slot and wire insulations in the 12/16 SRM [27]. According to IEEE 95-2002, the insulation should be capable of handling twice the maximum DC link voltage plus 1000 V. The 0.13 mm Nomex-410 insulation has breakdown voltage of 3575 V. Therefore, the 0.13 mm-thick Nomex-410 insulation layer used in the PMSM is considered for the stator slots. Furthermore, the Nomex-410 can withstand up to 250 °C [28].

Table 6. Proposed winding configuration and axial length constraints.

Parameter	Value
Number of turns per coil (N_t)	32
Number of strands	3
Wire fill factor	58.4%
Maximum current density	10.96 A/mm^2
Wire gauge	17 AWG heavy-build
Coil resistance (R_{coil})	0.02768 Ω
Stator core stack length (L_{stk})	47 mm
Estimated stacking factor	97%
Estimated end turn length (L_{end})	9.7 mm
Total axial length (L_{ax})	66.4 mm

The stack length of the SRM design is longer than the stack length of the PMSM. However, the PMSM design uses a Halbach magnet array design to improve the torque density and the maximum magnet temperature is considered as 120 °C. In the 12/16 SRM, there are no permanent magnets. Hence, the SRM can operate at a higher temperature. Among the active materials of an SRM, the polymer insulation of the magnet wires is usually more sensitive to temperature. The heavy-build MW-16C magnet wires that can withstand up to a maximum temperature of 240 °C are considered for the stator coils. The MW-16C magnet wires have 10,400 V breakdown voltages, which satisfies the IEEE 95-2002 standard [29]. Another temperature-limiting material in the PMSM design is the epoxy used for bonding the cores. In the PMSM design, the stator and rotor cores were made of cobalt–iron magnetic material. The laminations were bonded using EB-548 epoxy, which has a maximum allowable temperature of 140 °C. Spot welding is used to improve the structural integrity of the bonded laminations. The stator of the PMSM is also encapsulated using a potting material. The 12/16 SRM is also designed for cobalt–iron magnetic material, and it might require a similar core stacking technique using a bonding agent, potting material, and spot welding. A higher operating temperature for the SRM can be targeted with a higher-temperature epoxy for bonding the laminations or another stacking method such as welding or interlocking. The choice of stack retention method depends on various factors including manufacturability, impact on core loss, and production volume.

Table 7 compares the key design parameters of the SRM design with the benchmark PMSM design. It is worth noting that the efficiency of the SRM is obtained based on the losses calculated using JMAG software.

Table 7. Comparison of the SRM design with benchmark PMSM design.

Design Parameters	SRM Design	PMSM Design
Outer diameter	156.45 mm	156.45 mm
Axial length	66.4 mm	51.5 mm
Torque density	19.3 Nm/L	24.2 Nm/L
Current density	10.96 A/mm^2 (<11 A/mm^2)	10.7 A/mm^2 (<11 A/mm^2)
Fill factor	58.4% (<60%)	58.4% (<60%)
Efficiency	95.46%	96%

4.5. Thermal Analysis

Thermal analysis is conducted in MotorCAD software for the peak torque condition of 24 Nm at 5450 rpm. The thickness of the motor housing (heatsink) is 5 mm. The ambient temperature is considered as 60 °C. The DC copper losses in the windings are 460 W at 60 °C. The total iron loss calculated in JMAG is 191 W. Same materials used for the PMSM design in [20] are utilized in the thermal analysis. The thermal conductivities of the materials are shown in Table 8.

Table 8. Thermal conductivities of materials used in the thermal analysis.

Component	Material	Thermal Conductivity
Housing (heatsink)	Aluminum 2024-T3	120 W/m^2
Stator and rotor	Hiperco-50	20 W/m^2
Windings	Copper	400 W/m^2
Stator slot voids	Epoxy resin	1 W/m^2
Slot linear	Nomex 410	0.14 W/m^2

The steady-state temperature distribution in the motor is shown in Figure 12.

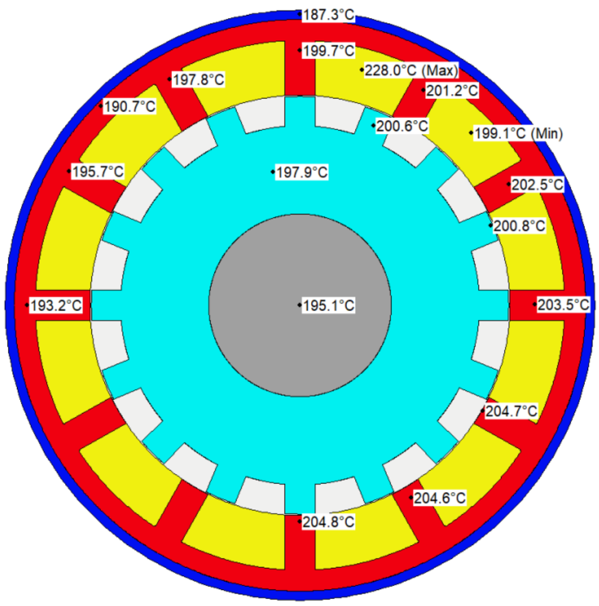

Figure 12. The steady-state temperature of the motor computed in MotorCAD.

As shown in Figure 12, the maximum winding temperature at the peak operating condition is 228 °C. The MW-16C magnet wires have a maximum temperature of 240 °C [29]. This confirms there will not be a thermal runaway during peak operation. The motor should be able to deliver peak power for 40 s during take-off [30]. According to [30], the maximum operation time of the motor during the take-off is 130 s. A transient thermal analysis is conducted until the winding temperature reaches its maximum during the peak torque condition of 24 Nm at 5450 rpm. As shown in Figure 13, the hotspot temperature during winding reaches 228 °C after 1.3 h. After 130 s, hotspot winding temperature reaches 106 °C.

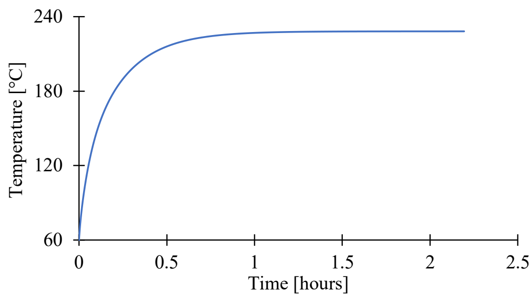

Figure 13. The temperature variation in the hotspot during winding under peak operating conditions.

5. Static Characteristics of the Proposed SRM Geometry

In this section, the static characteristics, such as the static flux linkage, magnetic flux density, static electromagnetic torque, and static induced voltage obtained from the MEC model of the proposed 12/16 SRM geometry are presented. The static characteristics of the proposed SRM are determined by constant current excitation applied to one-phase winding. The results are validated by using the FEM model of the proposed motor geometry in JMAG software.

5.1. Magnetic Flux Density

After obtaining the field solution, the branch fluxes in all mesh elements in the MEC model can be calculated using [18]

$$\boldsymbol{\phi}_b = \boldsymbol{L}\boldsymbol{\phi}_l \tag{7}$$

where $\boldsymbol{\phi}_b$ and $\boldsymbol{L}$ are the branch flux vector and loop matrix, respectively. Hence, the radial and tangential flux densities of the e^{th} mesh element can be determined by [18]

$$B_{rad,e} = \sqrt{\frac{\phi_1^2 + \phi_2^2}{2A_{rad,e}^2}},\ B_{tan,e} = \sqrt{\frac{\phi_3^2 + \phi_4^2}{2A_{tan,e}^2}} \tag{8}$$

where $A_{rad,e}$ and $A_{tan,e}$ are the cross-section areas of the mesh elements along the radial and tangential directions. The magnitude of the flux density is calculated by

$$B_e = \sqrt{B_{rad,e}^2 + B_{tan,e}^2}. \tag{9}$$

The airgap flux density components from the static analysis are shown in Figure 14. Flux densities are calculated for one stator pole pitch at the aligned and unaligned positions with a 60 A excitation current. The radial and tangential airgap flux densities from the MEC model match well with the FEM results. The radial flux density at the unaligned position and tangential flux density at the aligned position show minor differences near the spatial angles 10° and 20°. This is because of the field calculation error near the stator and rotor pole edges due to the complex elements. A complex element consists of both steel and air materials, as depicted in Figure 2 [18]. The accuracy of the airgap flux density can be further improved by increasing the number of mesh elements in the airgap and increasing the mesh element density near the stator and rotor pole edges.

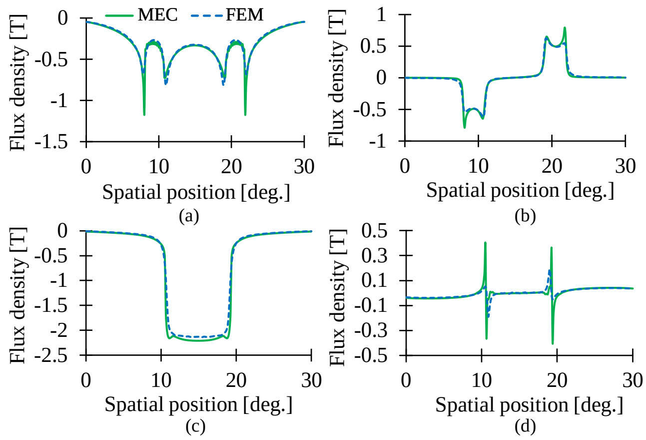

Figure 14. Airgap flux density waveforms at 60 A static excitation current: (**a**) radial flux density at the unaligned position, (**b**) tangential flux density at the unaligned position, (**c**) radial flux density at the aligned position, and (**d**) tangential flux density at the aligned position.

The magnitude of the flux density distribution inside the SRM at the aligned and unaligned positions is shown in Figure 15. The flux density distribution obtained from the MEC method shows fair agreement with the flux density distribution obtained from FEM. The flux density values at points P_1, P_2, and P_3 in Figure 15 and their percentage errors relative to the FEM are shown in Table 9. The maximum percentage error that occurred in the flux density calculation is less than 10%.

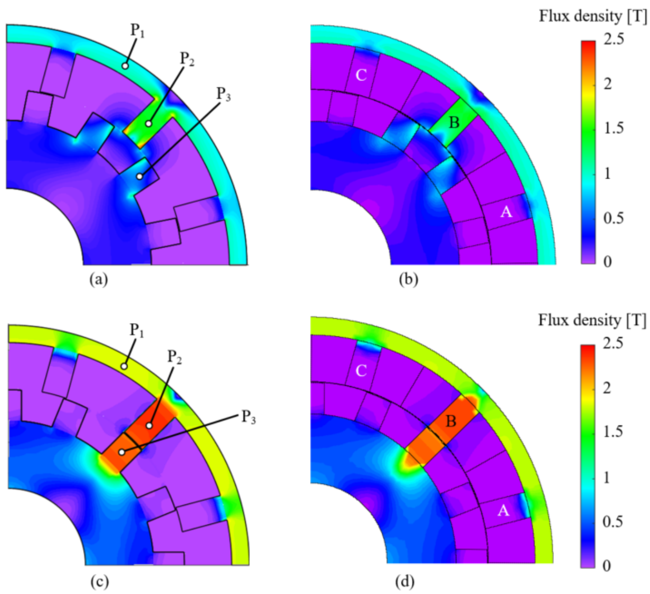

Figure 15. Magnetic flux density contours at 60 A static excitation current: (**a**) unaligned position, MEC, (**b**) unaligned position, FEM, (**c**) aligned position, MEC, and (**d**) aligned position, FEM.

Table 9. Flux density comparison at points P_1, P_2, and P_3 in Figure 15 in static simulations.

Position	Point P_1			Point P_2			Point P_3		
	MEC	FEM	% Error	MEC	FEM	% Error	MEC	FEM	% Error
Unaligned	0.98 T	0.96 T	2.1%	1.43 T	1.31 T	9.1%	0.55 T	0.54 T	1.9%
Aligned	1.89 T	1.8 T	5%	2.41 T	2.33 T	3.4%	2.31 T	2.25 T	2.7%

5.2. Static Flux Linkage, Torque and Voltage

The phase flux linkage vector $\boldsymbol{\psi}$ can be calculated using [18]

$$\boldsymbol{\psi} = p\mathbf{N}^T\boldsymbol{\phi}_l. \tag{10}$$

Hence, the induced phase voltage v_{ph} can be determined by

$$v_{ph} = r_{ph}i_{ph} + \frac{d}{dt}\psi_{ph} \tag{11}$$

where r_{ph}, i_{ph}, and ψ_{ph} are the phase resistance, phase current, and phase flux linkage, respectively. The Maxwell Stress Tensor method is applied to compute the tangential force density in the airgap. The electromagnetic torque is then calculated by integrating the tangential force density over the airgap surface area defined by the radial distance in the airgap circumference r_{fr} and the axial length, a [18]. For the 2D case, electromagnetic torque T can be expressed as a line integral:

$$T = p\nu_0 a \int_{l_{ag}} r_{fr}(B_{rad}\, B_{tan})dl \tag{12}$$

where B_{rad} and B_{tan} are the radial and tangential airgap flux densities. The line integral is evaluated along the arc length, l_{ag} in the airgap [18]. The variable ν_0 in Equation (12) denotes the reluctivity of air.

The static phase flux linkage of the proposed SRM geometry at different currents is shown in Figure 16. The flux linkage characteristics from the MEC method show a good match with the FEM results.

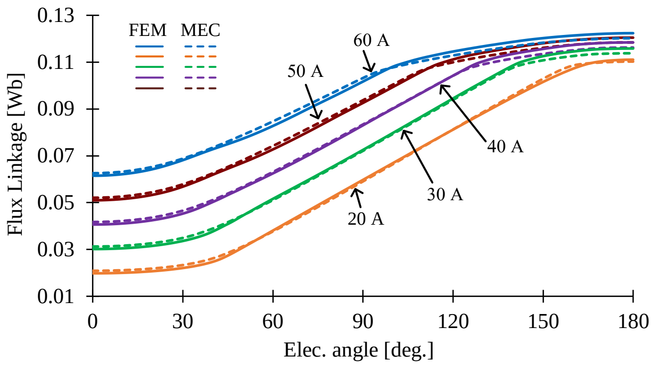

Figure 16. Static phase flux linkage characteristics at different currents.

The static induced voltage characteristics are shown in Figure 17. The induced voltage from the MEC model follows the voltage calculated from the FEM model. The voltage profile is calculated by taking the time derivative of the flux linkage characteristics from the MEC model. It can be observed from Figure 16 that the change in the slope in the flux linkage characteristics between electrical angles of 30° and 60° in the MEC model is not as smooth as the results from the FEM model. This is due to the coarse mesh density used in the MEC model. Therefore, voltage profiles from the MEC model do not match perfectly with the results from FEM within that interval. However, at the other electrical positions, the static voltage profiles from the MEC model match fairly well with the FEM results. It will be shown in the next section that this small difference in the static flux linkage and voltage characteristics does not cause a significant impact on the dynamic characteristics calculated from the MEC model.

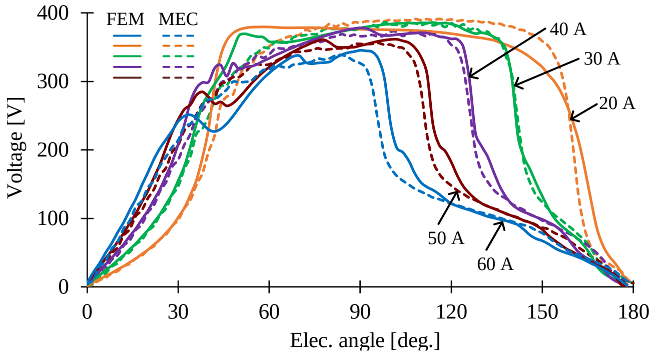

Figure 17. Static phase voltage characteristics at 5450 r/min at different currents.

The static electromagnetic torque characteristics of the 12/16 SRM geometry are shown in Figure 18. There is a good match between the torque calculated from the MEC and FEM models. Only minor differences can be recognized in the torque profiles between the electrical angles 30°–60°.

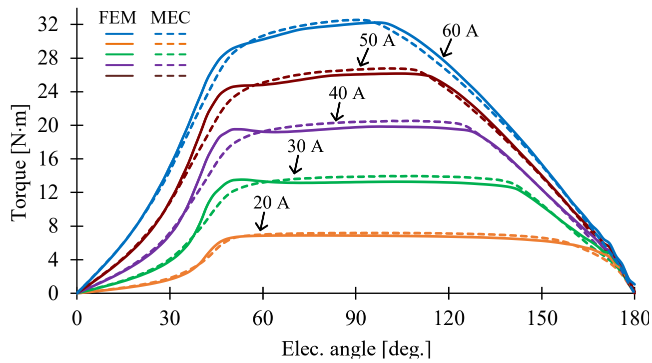

Figure 18. Static torque characteristics at different currents.

6. Dynamic Characteristics of the Proposed SRM Geometry

The dynamic phase currents and the corresponding flux density and electromagnetic torque from the MEC model of the proposed SRM geometry are presented in this section. The dynamic characteristics of the proposed SRM are obtained with the voltage excitation of all three phase windings. The current in the phase windings is regulated at a fixed reference using a hysteresis controller. The FEM model is developed in JMAG using the motor geometry obtained from the MEC-based design to validate the dynamic characteristics. The torque–speed characteristics and power–speed characteristics obtained using the MEC model are also presented and compared with FEM results.

6.1. Dynamic Current and Electromagnetic Torque

In the dynamic simulations, the conduction angles θ_{ON} and θ_{OFF} refer to the electrical angle of phase A. Zero electrical angle indicates that phase A is at the unaligned position. The dynamic current and corresponding electromagnetic torque at 2000 r/min and 4000 r/min are shown in Figures 19 and 20. The RMS current is regulated below 35 A. Here the conduction angles θ_{ON} and θ_{OFF} are heuristically adjusted to provide approximately 24 Nm of torque and the minimum possible torque ripple using the MEC model. The conduction angles are then applied to the FEM model, which is excited with an asymmetric bridge converter model with a DC link voltage source of 385 V. According to Figures 19 and 20, the dynamic phase current and electromagnetic torque determined from the MEC model are in good agreement with the FEM model. The calculated dynamic current and generated electromagnetic torque at 5450 rpm and 5460 r/min are shown in Figures 21 and 22. At both speeds, the RMS current is 34 A, as shown in

Figures 21a and 22a. The results from the MEC and FEM models show a good match. In some regions of the torque profiles in Figures 21b and 22b, the MEC model calculates slightly higher torque since the calculated dynamic current is higher in those regions. Furthermore, in some regions, the MEC model calculates a lower current compared with the FEM model. Hence, the generated torque in those regions is slightly less than the FEM results. The dynamic current and electromagnetic torque at 7000 r/min and 8000 r/min (high-speed operating points) are shown in Figures 23 and 24. As shown in Figures 23a and 24a, a hysteresis controller cannot regulate the current at the set reference due to the voltage dynamics at higher speeds. The MEC model can calculate the current fairly well in those conditions, compared with the FEM model. As shown in Figures 23b and 24b, the generated electromagnetic torque developed in the MEC model is in good agreement with the FEM model. The RMS current, average torque, peak–peak torque ripple, and percentage error relative to the FEM at different speeds are shown in Table 10. The percentage errors in Table 10 are caused due to field calculation errors in the MEC method. Field calculation errors in the MEC method mainly depend on the current, rotor position, turn on and turn off angles and DC link voltage. The design proposed from the MEC model has less than 5% error in the RMS current. The average torque calculation of the MEC-based design has a maximum error of 4.3%. At 2000 rpm, pk–pk torque ripple has higher error due to minor errors in the torque calculation, as shown in Figure 19. At other speeds, torque ripple has less than 10% error compared with the FEM results. At higher speeds, current cannot be regulated at the given reference due to the voltage dynamics. Therefore, the torque ripple is higher at higher speeds, as shown in Table 10.

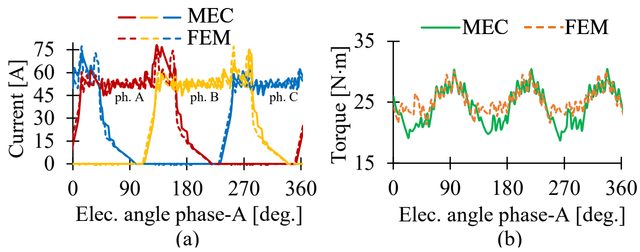

Figure 19. Dynamic characteristics at 2000 r/min at 385 V DC: (**a**) phase currents $I_{ref} = 52$ A, $\theta_{ON} = -5°$, and $\theta_{OFF} = 165°$ and (**b**) developed electromagnetic torque.

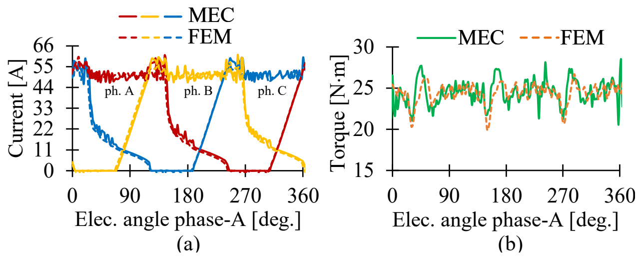

Figure 20. Dynamic characteristics at 4000 r/min at 385 V DC: (**a**) phase currents $I_{ref} = 50.5$ A, $\theta_{ON} = -50°$, and $\theta_{OFF} = 149°$ and (**b**) developed electromagnetic torque.

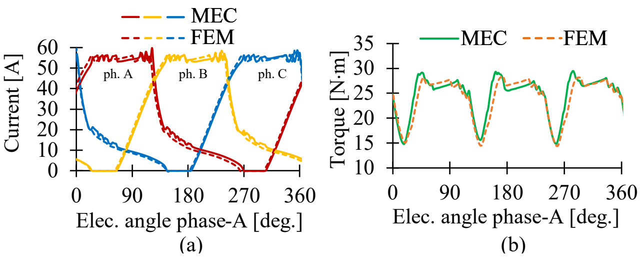

Figure 21. Dynamic characteristics at 5450 r/min at 385 V DC: (**a**) phase currents $I_{ref} = 55$ A, $\theta_{ON} = -52.5°$, and $\theta_{OFF} = 125°$ and (**b**) developed electromagnetic torque.

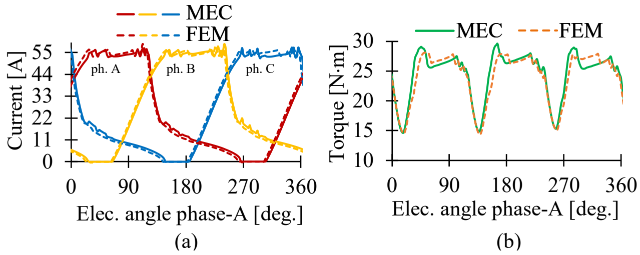

Figure 22. Dynamic characteristics at 5460 r/min at 385 V DC: (**a**) phase currents $I_{ref} = 55$ A, $\theta_{ON} = -52.5°$, and $\theta_{OFF} = 125°$ and (**b**) developed electromagnetic torque.

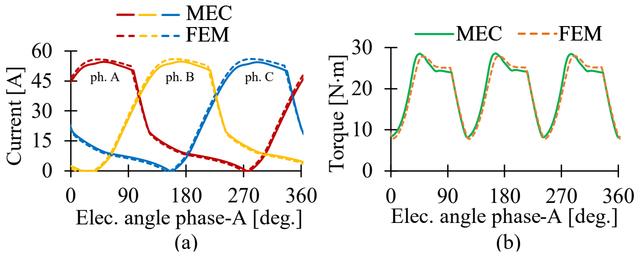

Figure 23. Dynamic characteristics at 7000 r/min at 385 V DC: (**a**) phase currents $I_{ref} = 55$ A, $\theta_{ON} = -79°$, and $\theta_{OFF} = 100°$ and (**b**) developed electromagnetic torque.

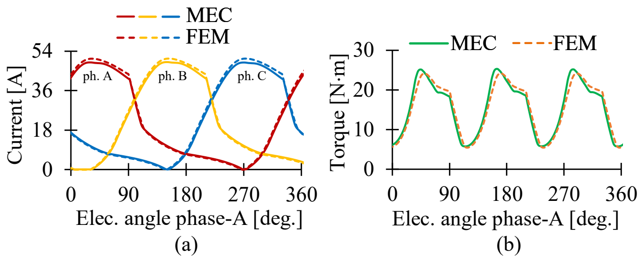

Figure 24. Dynamic characteristics at 8000 r/min at 385 V DC: (**a**) phase currents $I_{ref} = 55$ A, $\theta_{ON} = -85°$, and $\theta_{OFF} = 95°$ and (**b**) developed electromagnetic torque.

Table 10. Comparison of RMS current, average torque, and peak–peak torque ripple from the MEC and FEM models.

Speed	RMS Current			Avg. Torque			Pk–Pk Torque Ripple		
	MEC	**FEM**	**% Error**	**MEC**	**FEM**	**% Error**	**MEC**	**FEM**	**% Error**
2000 r/min	35.8 A	34.9 A	3.2%	24.2 N·m	25.3 N·m	4.3%	11.7 N·m	8.7 N·m	25.6%
4000 r/min	35.5 A	34.8 A	2%	24.5 N·m	24.4 N·m	0.6%	7.86 N·m	10.37 N·m	9.7%
5450 r/min	34.3 A	34.2 A	0.3%	24.4 N·m	24 N·m	2.5%	14.59 N·m	13.97 N·m	4.44%
5460 r/min	34 A	34.1 A	0.3%	24.4 N·m	24 N·m	2.5%	14.86 N·m	14.18 N·m	4.8%
6000 r/min	32 A	33. 6A	4.8%	23.4 N·m	23.5 N·m	0.4%	15.95 N·m	14.89 N·m	7.12%
7000 r/min	31.7 A	32.5 A	2.5%	20.1 N·m	19.9 N·m	1%	20.45 N·m	20.13 N·m	1.59%
8000 r/min	27.8 A	28.6 A	2.8%	15.7 N·m	15.6 N·m	0.6%	19.5 N·m	18.72 N·m	4.17%

6.2. Magnetic Flux Density

The radial and tangential magnetic flux densities can be computed using Equation (8). Figure 25 shows the radial and tangential flux density waveforms at the phase-A electrical position of $\theta_{elec,phA} = 240°$, for the operating conditions in Figure 21. At this position, phase C is the incoming phase, and phases A and B are the outgoing phases. Flux density waveforms from the MEC model match well with the FEM results. The magnetic flux density contours inside the motor can be calculated using Equation (9). Figure 26 shows the magnetic flux density contours of the 12/16 SRM design from the MEC and FEA models for the same electrical position. There is a good match between the flux density distributions obtained from the MEC and FEM models. Flux density values and percentage errors with respect to the FEM for points P_1, P_2, P_3, P_4, P_5, and P_6 in Figure 26a are given in Table 11.

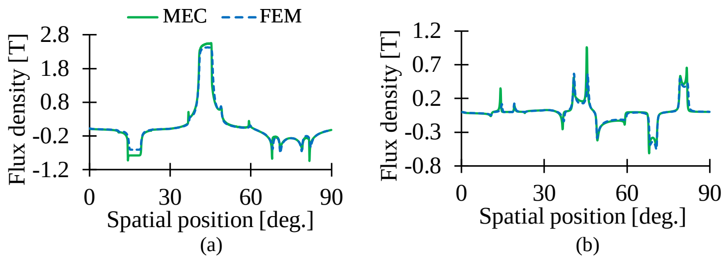

Figure 25. Airgap flux density at $\theta_{elec,phA} = 240°$ for phase currents in Figure 21: (a) radial component and (b) tangential component.

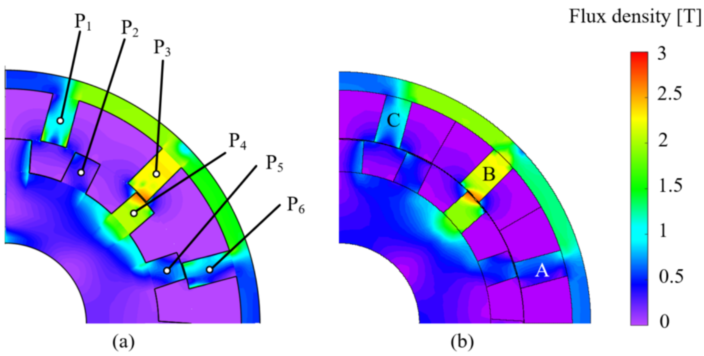

Figure 26. Magnetic flux density contours at $\theta_{elec,phA} = 240°$ for the current waveform in Figure 21.

Table 11. Flux density comparison at points P_1, P_2, P_3, P_4, P_5, and P_6 for the dynamic operation in Figure 26.

Location	MEC	FEM	% Error
Point P_1	1.01 T	0.89 T	13.5%
Point P_2	0.39 T	0.38 T	2.6%
Point P_3	2.24 T	2.26 T	0.9%
Point P_4	2.03 T	1.98 T	2.5%
Point P_5	0.61 T	0.52 T	17.3%
Point P_6	0.63 T	0.54 T	16.7%

6.3. Torque–Speed Characteristics of the 12/16 SRM

Figure 27 shows the torque–speed and power–speed characteristics of the proposed SRM geometry for the peak-load operation. The average torque values at different speeds in Table 10 are used in Figure 27a. The output power in Figure 27b is calculated using the average torque and rotation speed reported in Table 10. As shown in Figure 27, the calculated characteristics from the MEC-based model match well with the FEM results. As shown in Figure 27a, the proposed SRM can provide 24 N·m torque from 2000 r/min to 5460 r/min, which satisfies the design specifications. According to Figure 27b, the proposed geometry can produce 14.7 kW of maximum output power, and it exceeds the given requirement 13.7 kW with the minimum DC link voltage of 385 VDC.

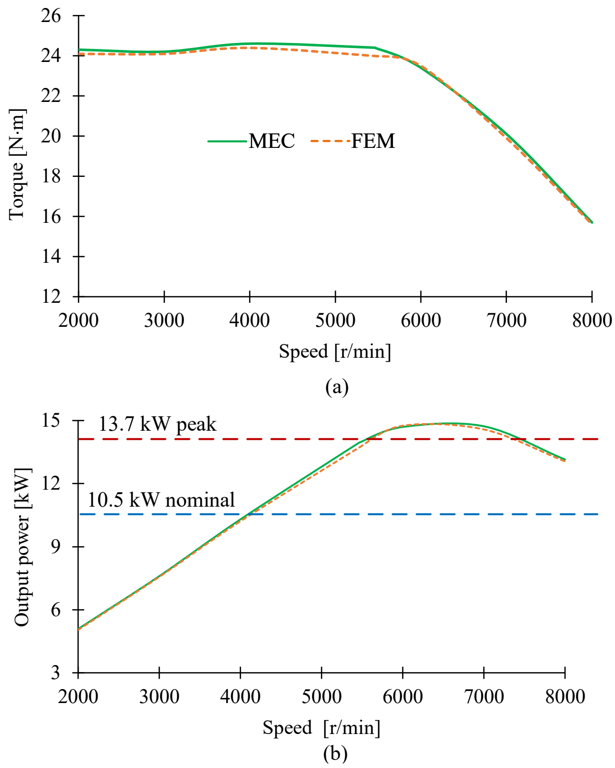

Figure 27. Motor characteristics for the peak operating point of the 12/16 SRM at 385 V DC link voltage: (**a**) torque–speed characteristics and (**b**) power–speed characteristics.

7. Conclusions

This paper presents the sizing of a three-phase 12/16 SRM proposed for the high-lift motor (HLM) application for the NASA Maxwell X-57 aircraft using the reluctance mesh-based MEC method. NASA designed a high-power-density PMSM using a Halbach magnet array according to defined performance and geometry constraints for the HLM. The 12/16 SRM can achieve 24 N·m at 5450 r/min with 385 V minimum DC link voltage within the design constraints given by NASA. The electromagnetic performance of the SRM and, hence, the reluctance mesh-based MEC model developed for the sizing of the SRM were validated using FEM. The results sufficiently match the ones from the FEM model. This paper demonstrates that the proposed MEC model is an effective tool for the sizing of a switched reluctance motor.

The stack length of the SRM stator core can be reduced further by allowing a current density that exceeds the design constraint of 11 A/mm^2. This can result in a higher operating temperature, but SRM can operate at a higher temperature than the PMSM due to the lack of permanent magnets. The obtained motor geometry of the 12/16 SRM using the MEC model should be further improved with more detailed FEM simulations. The losses and efficiency of the motor should be calculated in FEM. Thermal analysis is required to determine the operating temperature of the 12/16 SRM and validate that the stack length can be further reduced by enabling a higher current density operation.

Author Contributions: Conceptualization, G.W.; methodology, G.W.; software, G.W. and B.B.; validation, G.W. and B.B.; formal analysis, G.W.; investigation, B.B.; resources, G.W. and B.B.; original draft preparation, G.W.; review and editing, B.B.; visualization, G.W. and B.B.; supervision, B.B.; project administration, B.B. All authors have read and agreed to the published version of the manuscript.

Funding: This research received no external funding.

Data Availability Statement: Not applicable.

Acknowledgments: The authors would like to thank JSOL and Mathworks for their support with JMAG and MATLAB softwares in this research.

Conflicts of Interest: The authors declare no conflict of interest.

References

1. Sayed, E.; Abdalmagid, M.; Pietrini, G.; Sa'adeh, N.M.; Callegaro, A.D.; Goldstein, C.; Emadi, A. Review of electric machines in more/hybrid/turbo electric aircraft. *IEEE Trans. Transp. Electr.* **2021**, *7*, 2976–3005. [CrossRef]
2. Sahoo, S.; Zhao, X.; Kyprianidis, K. A review of concepts, benefits, and challenges for future electrical propulsion-based aircraft. *Aerospace* **2020**, *7*, 44. [CrossRef]
3. Bilgin, B.; Jiang, J.W.; Emadi, A. Electric motor industry and switched reluctance machines. In *Switched Reluctance Motor Drives: Fundamentals to Applications*; CRC Press: Boca Raton, FL, USA, 2018; pp. 1–31.
4. Watthewaduge, G.; Sayed, E.; Emadi, A.; Bilgin, B. Electromagnetic Modeling Techniques for Switched Reluctance Machines: State-of-the-Art Review. *IEEE Open J. Ind. Electron. Soc.* **2020**, *1*, 218–234. [CrossRef]
5. Bilgin, B.; Liang, J.; Terzic, M.V.; Dong, J.; Rodriguez, R.; Trickett, E.; Emadi, A. Modeling and analysis of electric motors: State-of-the-art review. *IEEE Trans. Transp. Electr.* **2019**, *5*, 602–617. [CrossRef]
6. Li, S.; Zhang, S.; Habetler, T.G.; Harley, R.G. Modeling, design optimization, and applications of switched reluctance machines-a review. *IEEE Trans. Ind. Appl.* **2019**, *55*, 2660–2681. [CrossRef]
7. Tang, Y.; Paulides, J.J.; Lomonova, E.A. Automated design of DC-excited flux-switching in-wheel motor using magnetic equivalent circuits. *IEEE Trans. Magn.* **2015**, *51*, 1–11. [CrossRef]
8. Delale, A.; Albert, L.; Gerbaud, L.; Wurtz, F. Automatic generation of sizing models for the optimization of electromagnetic devices using reluctance networks. *IEEE Trans. Magn.* **2004**, *40*, 830–833. [CrossRef]
9. Ostovic, V. Magnetic circuits. In *Dynamics of Saturated Electric Machines*; Springer Science & Business Media: Berlin/Heidelberg, Germany, 2012; pp. 5–28.
10. Yilmaz, M.; Krein, P.T. Capabilities of finite element analysis and magnetic equivalent circuits for electrical machine analysis and design. In Proceedings of the 2008 IEEE Power Electronics Specialists Conference, Rhodes, Greece, 15–19 June 2008; pp. 4027–4033.
11. Lee, J.J.; Lee, J.; Kim, K.S. Design of a WFSM for an electric vehicle based on a nonlinear magnetic equivalent circuit. *IEEE Trans. Appl. Supercond.* **2018**, *28*, 5206304. [CrossRef]
12. Lee, J.G.; Lim, D.K.; Jung, H.K. Analysis and design of interior permanent magnet synchronous motor using a sequential-stage magnetic equivalent circuit. *IEEE Trans. Magn.* **2019**, *55*, 7501004. [CrossRef]
13. Ullah, N.; Khan, F.; Ullah, W.; Umair, M.; Khattak, Z. Magnetic equivalent circuit models using global reluctance networks methodology for design of permanent magnet flux switching machine. In Proceedings of the 2018 15th International Bhurban Conference on Applied Sciences and Technology (IBCAST), Islamabad, Pakistan, 9–13 January 2018; pp. 397–404.
14. Labak, A.; Kar, N.C. Designing and prototyping a novel five-phase pancake-shaped axial-flux SRM for electric vehicle application through dynamic FEA incorporating flux-tube modeling. *IEEE Trans. Ind. Appl.* **2013**, *49*, 1276–1288. [CrossRef]
15. Ma, J.; Qu, R.; Li, J. Optimal design of axial flux switched reluctance motor for electric vehicle application. In Proceedings of the 2014 17th International Conference on Electrical Machines and Systems (ICEMS), Hangzhou, China, 22–25 October 2014; pp. 1860–1865.
16. Watthewaduge, G.; Sayed, E.; Bakr, M.; Emadi, A.; Bilgin, B. An optimization study for a switched reluctance motor using magnetic equivalent circuit and space mapping techniques. In Proceedings of the 2020 IEEE Transportation Electrification Conference & Expo (ITEC), Chicago, IL, USA, 23–26 June 2020; pp. 1025–1030.
17. Hemeida, A.; Lehikoinen, A.; Rasilo, P.; Vansompel, H.; Belahcen, A.; Arkkio, A.; Sergeant, P. A simple and efficient quasi-3D magnetic equivalent circuit for surface axial flux permanent magnet synchronous machines. *IEEE Trans. Ind. Electron.* **2018**, *66*, 8318–8333. [CrossRef]
18. Watthewaduge, G.; Bilgin, B. Reluctance mesh-based magnetic equivalent circuit modeling of switched reluctance motors for static and dynamic analysis. *IEEE Trans. Transp. Electr.* **2021**, *8*, 2164–2176. [CrossRef]
19. Hall, D.; Chin, J.; Anderson, A.; Smith, A.; Edwards, R.; Duffy, K.P. Development of a Maxwell X-57 high lift motor reference design. In Proceedings of the AIAA Propulsion and Energy Forum, Indianapolis, IN, USA, 19–22 August 2019; pp. 4481–4502.
20. Schnulo, S.L.; Hall, D.L.; Chin, J.C.; Smith, A.D. Further development of the NASA X-57 Maxwell mission planning tool for mods II, III, and IV. In Proceedings of the 2019 AIAA/IEEE Electric Aircraft Technologies Symposium (EATS), Indianapolis, IN, USA, 22–24 August 2019; pp. 1–14.
21. Bilgin, B.; Jiang, J.W.; Emadi, A. Derivation of pole configuration in switched reluctance machines. In *Switched Reluctance Motor Drives: Fundamentals to Applications*; CRC Press: Boca Raton, FL, USA, 2018; pp. 91–121.
22. Howey, B.; Bilgin, B.; Emadi, A. Design of an external-rotor direct drive e-bike switched reluctance motor. *IEEE Trans. Veh. Technol.* **2020**, *69*, 2552–2562. [CrossRef]
23. Hiperco-50 Datasheet. Carpenter. 2020. Available online: https://www.carpentertechnology.com/alloy-finder/hiperco-50a (accessed on 8 February 2022).
24. AFK-502 Datasheet. Aperam. 2021. Available online: https://www.aperam.com/product/imphy-afk-502 (accessed on 8 February 2022).

25. Vacodur-49 Datasheet. Vacuumschmelze. 2021. Available online: https://vacuumschmelze.com/products/soft-magnetic-materials-and-stamped-parts/49-Cobalt-Iron---VACOFLUX-and-VACODUR (accessed on 8 February 2022).
26. JFE N-Core Datasheet. JFE. 2003. Available online: https://www.jfe-steel.co.jp/en/products/electrical/product/n_core.php (accessed on 8 February 2022).
27. *ANSI/IEEE Std 95-2002*; Recommended Practice for Insulation Testing of AC Electric Machinery (2300 V and Above) with High Direct Voltage. IEEE: Manhattan, NY, USA, 2002.
28. NOMEX-410 Technical Data Sheet. Dupont. 2016. Available online: https://www.dupont.com/products/nomex-400-series.html (accessed on 8 February 2022).
29. Essex Wire Datasheet. Essex Brownell. 2008. Available online: https://www.essexbrownell.com/media/cms_content/downloads_links/Allex-EN.pdf (accessed on 8 February 2022).
30. Edwards, R.; Smith, A. Design and test of a structurally-integrated heat sink for the Maxwell X-57 high lift motor controller. In Proceedings of the Thermal & Fluids Analysis Workshop, Hampton, VA, USA, 26–30 August 2019; Number GRC-E-DAA-TN72618.